

Seismic Zone at East Africa Rift: Insights into the Geothermal Potential

Ezer Patlan^{1,2}, Aaron. A. Velasco², Antony Wamalwa³, and Galen Kaip²

Now at ¹USGS, 345 Middlefield Rd. MS 977, Menlo Park, CA 94025, USA

epatlan@usgs.gov

²The University of Texas at El Paso (UTEP), 500 West University Ave., El Paso, TX 79968, USA

velasco@geo.utep.edu; gkaip@utep.edu

³Geothermal Development Company (GDC), Kenyatta Ave. Generation Building, P.O. Box: 17700-20100, Nakuru, Kenya

awamalwa@gdc.co.ke

Keywords: Seismicity, Stress Analysis, and Tomography

ABSTRACT

The East African Rift System (EARS) within Kenya has been previously studied for its potential for geothermal energy production. EARS, an active continental rift zone, contains a number of active and inactive volcanoes that may be potential sites for geothermal energy production. The University of Texas at El Paso and the Kenyan Geothermal Development Company (GDC) collaborated to monitor several volcanic centers by deploying 14 seismic stations around the Menengai Caldera and nine stations at the volcanic centers: Silali, Paka, and Korosi. We perform double-difference relocations to obtain high precision earthquake locations, and identify three major seismic swarms located in two volcanic systems. Two of them occur at the center of Menengai, one with a pipe-like shape and one on the northwestern flank with a circular pattern of seismicity. A third swarm is located at the center of Paka volcano and shows a pipe-like pattern of seismicity at the summit of the crater. Korosi volcano shows no seismic activity during this study. We also estimate the stress conditions of the swarms using Gutenberg-Richter b -value analyses to interpret the variation in stresses accompanying the migration of fluids and the tectonic stress state. One seismic swarm in Menengai occurred at the center of the caldera with an increase of b -value ($b=1.24$) and another swarm on the northwestern flank has a lower b -value ($b=1.76$), which we interpret as being due to magmatic fluid flow generating high temperature and pore pressure. For the third swarm at Silali volcano, the b -value is also lower ($b=0.83$) and attributed also to the regional tectonic stress conditions. We further use focal mechanisms to approximate the orientation of stress and whether faulting is modulated by local stresses. We find that P-axis strikes NE-SW for two seismic swarms beneath the Menengai and Paka volcano. To further resolve the geometries and locations of the magmatic reservoirs at the four volcanic centers, we develop a 3-D high-resolution S -wave velocity model, which delineates the locations and shapes of the sources of the magmatic reservoirs as well as the stress perturbations due to these processes. The tomography model extends throughout the four volcanic systems, and we identify four magma chambers at approximately 6 km in depth, consistent with the seismicity results. We conclude that active fluid movement under Menengai and Paka indicated by seismicity and low S -wave velocity suggest potential for geothermal production at these sites.

1. INTRODUCTION

The EARS has been explored for potential geothermal resources for some time (Tongue, 1991; Tongue et al, 1994; Simiyu, 2009; Wamalwa et al., 2013; Young et al., 1991). These potential geothermal resources are thought to collocate with active and passive volcanic centers along the extent of the EARS (Ibs-von Seht et al., 2001 and 2007; Tongue et al., 1994). To investigate the potential for geothermal resources the University of Texas at El Paso (UTEP) and the Geothermal Development Company (GDC) collaborated to monitor several volcanic centers starting in March 2011 through 2014. This collaboration includes passive seismic sensor deployments and a controlled source experiment. At one of the volcanic centers, Menengai caldera, 14 seismic sensors were deployed around the caldera. At north end of the EARS in Kenya, three volcanic systems Silali, Paka, and Korosi volcanoes nine seismic sensors were deployed. The southern portion of the Kenya rift has been the target of a number of recent geophysical and geological investigations, including: teleseismic tomography (Mulibo and Nyblade, 2013); Interferometric Analysis of Synthetic Aperture Radar (InSAR) studies (Biggs et al., 2009); shear-wave splitting analysis (Walker et al., 2004; Bagley and Nyblade, 2013); micro-seismic relocation (Simiyu and Keller, 2001; Simiyu, 2009); and ambient noise tomography (Kim et al., 2012). Biggs et al. (2009) and Ebmeier et al. (2013) identified active deformation at the Menengai Caldera and Silali-Paka-Korosi volcanoes between 2007 and 2010.

Ever since geological and geophysical studies were first carried out in the Kenya Rift, the rift has been known as a region of high geodynamic activity expressed by recent volcanism, geothermal activity and a high rate of seismicity. Molnar & Aggarwal (1971) carried out the first microseismic in the Magadi Rift, located in southern Kenya. The seismic activity was located within the rift zone and aligned with regional tectonic faults. Whereas the study of Ibs-von Seht et al. (2001) focused in the Magadi rift and found a seismic swarm with approximated b -value of 0.75 indicating a strong crust and tectonic origin. From their analysis, Ibs-von Seht et al. (2001) derived focal mechanisms in the region and found WNW-ESE-directed tensional stress field that corresponds with Kenya rift. The results of Ibs-von Seht et al. (2001) were in agreement with previous studies (Tongue et al., 1994) and concluded predominantly normal

faulting on fault planes aligned parallel to the rift valley axis, and a minor fraction of strike-slip mechanism is affiliated with an extensional stress field. Another study conducted by Tongue (1991), as part of the Kenya Rift International Seismic Project (KRISP 85), utilized a temporary seismic network in the vicinity of Lake Bogoria. Tongue (1991) for P-wave tomography in an effort to investigate the geothermal activity around the southern shores of the lake. The studies evaluated different sites around the Kenya rift system for decades to understand the volcanic and rift process in the EARS. In summary, seismic swarms are attributed to shallow faults, preexisting faults beneath the rift or in connection with dyke intrusions. The authors also applied seismic tomography to examine the velocity structure of the upper crust to understand geothermal and volcanic processes.

In this paper, Menengai Caldera and Silali-Paka-Korosi volcanoes are, therefore, a suitable sites to study the geothermal and volcanic processes within the EARS. We analyze the seismic events around the Menengai caldera and Silali-Paka-Korosi volcanoes to identify faults that may serve as conduits for fluid and heat — necessary components for exploiting geothermal energy (Simuyi and Keller, 2001; Wamalwa et al., 2013). For this purpose, a temporary seismic network was installed and operated for three years. The experiment was designed to undertake a detailed investigation of the local seismicity including precise earthquake location to estimate the earthquake size distribution and identify active fault systems. In particular, we perform the double-difference location (Waldhauser and Ellsworth, 2000) and located three hypocenter clusters, determine focal mechanisms to carry out a stress field analysis (Tongue, 1991 and Tongue et al., 1994; Mulibo and Nyblade, 2009), and a Gutenberg-Richter *b*-value analysis to better interpret the variation in stresses accompanying the migration of fluids and the tectonic stress state (Bridges and Gao et al., 2006). We perform a high-resolution 3-D ambient noise tomography analysis (Bensen et al., 2007), using data from 20, mainly broadband, seismic stations recorded at two different seismic networks deployed at Silali, Paka, Korosi, and Menengai Caldera to construct a 3D velocity model for the upper crust of the northernmost of the Kenya rift.

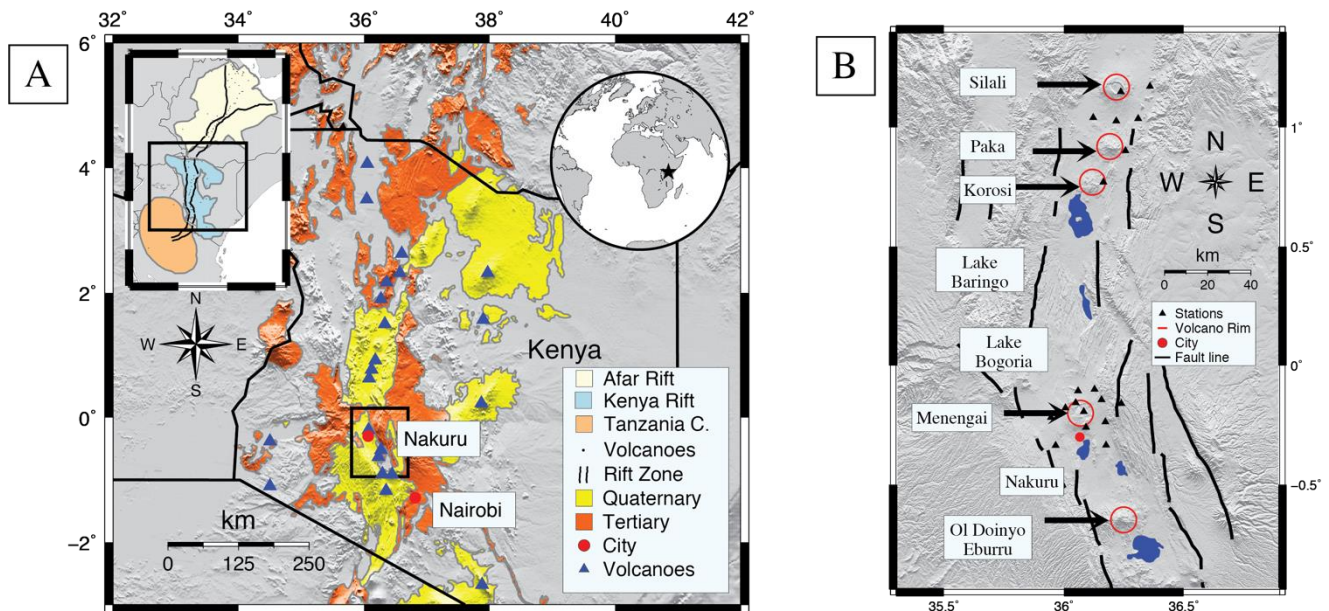


Figure 1: (A) Regional tectonic setting of EARS. In the inset, the bold line shows the rift zone of EARS: colors indicate the individual tectonic rift systems of EARS: Afar rift (yellow), Kenya rift (blue), and Tanzania craton (orange). Main map: yellow and orange represent the Quaternary and Tertiary volcanics, respectively, of the EARS (Persits et al., 2002). (B) Main map: bold lines indicating the rift zone. Black triangles represent the seismic network, and the open red circle illustrate the flank of the volcano.

2. GEOLOGY AND PREVIOUS GEOPHYSICAL STUDIES

During the last 40 to 30 million years (Myr) ago, a super swell occurred along the East African Rift System (EARS) resulting in elevated topography, evolving from a complex pattern of mantle circulation and rift plume (Roberts et al., 2012; Rooney et al., 2014). As the EARS initiated, two plateaus called Ethiopia Domes (Afar rift) and Kenya Domes (Kenya rift and Tanzania craton) formed (Rooney et al., 2014) (Figure 1). Early volcanism began approximately 30 to 20 Myr ago between the Ethiopia and Kenya domes, separated by the low-lying Turkana depression. Currently, the EARS has significant heat flow, high-elevation (~3000 km), and spreading rate of 2.1 mm/yr, which is attributed to uplift and/or rift initiation (Chorowicz, 2005; Halldörsson et al., 2014; Simiyu, 2009). Begg et al. (2009) found evidence that the lithosphere accretion in the Kenya Domes is strongly affected by the thermal overprint of the EARS. The volcano-tectonic activity in the EARS with ages of 8-5 Ma is found in between the border of Kenya Rift and Tanzania Craton (Albaric et al., 2014) (Figure 1). The most recent volcanic activity in the Kenya rift system occurred about 180 years BC (Clarke et al., 1987). Menengai Caldera is built of trachyte lavas and has been active since about 0.8 Myr to present (Simiyu, 2010). The caldera has steep sides of up to 300 m high where old shield lavas are exposed, and pyroclastics and tuffs cover the rest of the area outside the caldera. The earliest eruption activity at Silali has been estimated to be no more than few hundred years old (Williams et al., 1984). At Paka volcano the most recent eruptions occurred 10 Ka and there is widespread fumarolic activity, and hydrothermally altered rocks

(Simiyu 2010). The composition of the Silali-Paka-Korosi volcanoes show evidence of basalt flows and pyroclastic material (Williams et al., 1984; Simiyu 2010).

3. DATA AND PROCESSING

The GDC and researchers from the Department of Geological Sciences at UTEP installed a total of fourteen seismometers around the Menengai caldera region. The passive seismic deployments in the region were conducted in two distinct phases. Phase 1 was deployed in the Menengai caldera in March 2011 installing seven temporal seismic stations, and Phase 2 was completed in August 2012 with the installment of seven additional stations located outside Menengai (Table 1). The Menengai network used a variety of sensors including Guralp 40T and 3T sensors and Miniseis sensors, while the Silali-Paka-Korosi network consisted of nine stations with Guralp 3T sensors (120 seconds to 30-Hz frequency) (Table 1). The seismic stations were installed on public and private property (schools and private homes) for security. We converted the data from RefTek to miniseed format, manually evaluated the GPS time-stamp, and reviewed waveform data to see if there were any offset or timing issues. We flagged the time windows that showed evidence of timing issues or had no recorded GPS time. We archived the miniseed data into an Antelope database from Boulder Real Time Technologies (BRTT), utilizing this software package to analyze the data. The data is archived at the Incorporated Research Institutions for Seismology (IRIS) Data Management Center (DMC) and available to the public (Velasco et al., 2011).

Table 1: Site location for the 1C Network

Station Code	Lat.	Lon.	Elev.	(m)	Sensor	Description
ANR	-0.182	36.2446	2730		40T	Nknyami School
BHT	-0.143	36.1573	2115		3T	Bahati School
BLS	-0.114	35.1598	2173		40T	Brightlight School
DIRG	-0.096	35.0964	1700		3T	Digor Homestead
GSSH	-0.159	36.2398	2711		40T	Menengai Caldera
KIMU	-0.266	36.0248	1946		3T	Kiamunyi Academy
LWHS	-0.222	36.1767	2068		3T	Lockwood School
MCN1	-0.193	36.0829	1872		HS10	Menengai Crater
MNP	-0.217	35.9465	1991		40T	Primary School
NDG	-0.106	36.0593	2068		40T	Ndigiri School
RGO	-0.156	36.0493	1961		HS10	Rigogo School
SLS	-0.099	36.1279	1838		40T	Solai School
TOR1	-0.177	36.0067	1946		HS10	Toroitich
VWP	-0.259	36.0925	2099		40T	View Point
AKWI	1.0368	36.3100	871.9		3T	NE Paka
KAPD	1.1852	36.1052	723.0		3T	W Silali
KTG	0.9018	36.2570	1216.0		3T	E Paka
MOND	0.8962	36.0859	883.0		3T	W Paka
NAK	0.7701	36.1650	1031.0		3T	E Korosi
NASO	1.1719	36.3591	936.0		3T	E Silali
NATN	1.0410	36.1226	799.0		3T	SW Silali
NAUD	1.0268	36.2187	873.0		3T	N Paka
SIL	1.1492	36.2379	1001.0		3T	Silali's Crater

4. METHODOLOGY

4.1 Double Difference Earthquake Relocation

We aim to identify active fault and fracture system within the volcanic center, which can be done by using high precision microseismic locations. To accomplish high precision earthquake locations, we apply the double-difference (HypoDD) earthquake location method (Waldhauser and Ellsworth, 2000) at the Menengai network. Double difference relocations utilizes arrival time and waveform similarity of nearby earthquakes to relatively locate the events, thereby removing errors associated with the usually poorly known velocity structure. We manually pick the P arrival time for every event previously determined and then compute a cross-correlated time pick for all events and stations. In order to evaluate the location of the events, a 1-D velocity model from Simuyi and Keller (2000) is used in the inversion as an initial model.

4.2 Local Magnitude and b-value Analysis

We approximate the local magnitude (M_L) using the distance between the station and event (Δ), and the maximum amplitude (A) of the event (Geiger, 1912):

$$M_L = \log_{10}(A) + 2.76\log_{10}(\Delta) - 2.48 \quad (1)$$

We determine local magnitudes (ML) in the range between 1.42 and 3.47 for the 198 earthquakes located using double difference earthquake location (Figure 2). The majority of earthquakes in both clusters range from M_L of 1.4 to 3.4 at Menengai caldera and one cluster range between -1 and 3.98 for 519 events at Paka volcano (Figure 3).

In order to determine how magnitudes are distributed and how to establish cutoff magnitudes, we use the frequency-magnitude distribution (FMD) (Gutenberg and Richter, 1944; Hamlyn et al., 2014; Ebinger et al., 2008). The frequency-magnitude distribution originates from the power-law relationship between the frequency of occurrence and magnitude of earthquakes:

$$\log(N) = a - bM \quad (2)$$

where N is the cumulative number of earthquakes with magnitude larger than M , and a and b are constants. We use the maximum-likelihood method (Utsu, 1965) to calculate the b-value,

$$b = \frac{\log_{10}e}{M_a - M_c} \quad (3)$$

where M_a is the average magnitude and M_c is the cutoff magnitude. It has been shown in laboratories, mines, and numerical simulations that the slope of the frequency-magnitude distribution curve, or b-value, depends on stress conditions (Murru et al., 2007; Sánchez et al., 2004; Utsu, 1965).

4.3 Focal Mechanism

We compute lower hemisphere focal mechanism to constrain the orientation of crustal stresses using HASH (Hardebeck and Shearer, 2002; 2003) for earthquakes with a magnitude range from 1.0 to 3.0. The program uses the station locations, take off angles using iasp91 velocity model (Kennett 1991), and P-wave polarity to perform a grid search for the best-fit double-couple solution (Hardebeck and Shearer, 2002; 2003, Ebinger et al., 2008). We are able to estimate 29 robust fault plane solutions for the clusters. For each double-couple source model obtained, events with four polarities or more are considered for calculations. These solutions are classified in a wide range of faulting mechanisms based on the angle of P-axes and T-axes plunges. We use an event classification (normal, transtensive, strike-slip, transpressive, and reverse faulting) to characterize different types of focal components (Andronicos et al., 2007).

4.4 Ambient Noise Tomography

In this study, we image the shallow crust of the four volcanic systems using ambient noise tomography on continuous data from the Menengai and Silali-Paka-Korosi seismic broadband network (Velasco et al., 2011). Specifically, we develop the corresponding Green's functions and determine group velocities between all station combinations. We then invert these group velocity curves to develop group velocity maps, invert for 1-D S-velocity structure at each cell of our model, test for sensitivity, and produce a 3-D velocity model for the region (Goutorbe et al., 2015; Fang et al., 2015; Spica et al., 2015).

To apply this method, we: 1) remove the instrumentation response from the Guralp 40T, Guralp 3T, and HS10 sensors, using band-pass filters appropriate for each station pair; 2) remove the earthquake signals by applying a one-bit normalization (Bensen et al., 2007); 3) perform spectral whitening to reduce the seismic amplitude and/or to flatten the spectral over the entire period band (Bensen et al., 2007; Yang et al., 2011; Yang, Shen, and Ritzwoller, 2011); 4) retrieve the Green's function by cross-correlating the normalized waveforms between two seismic stations in one hour increments; and 5) stack all months into bins and estimate the group velocity uncertainties (Campillo and Paul 2003; Nicolson et al., 2012). We apply frequency time analysis (Herrmann and Ammon, 2004; Levshin et al., 1972) to measure the dispersion curves of the Rayleigh waves. The Rayleigh wave dispersion measurements are used to invert for group velocity maps, at periods 1 to 8 s on a $0.02^\circ \times 0.02^\circ$ grid for the Menengai Caldera and its surrounding region implementing the tomographic method of Pasyanos et al., (2007) and Pasyanos (2008). This technique, based on a grid-search method, is used to solve for lateral variation in group velocity.

We then construct a grid to approximate 1-D shear velocity inversion, inverting the group velocity (1 – 8 s) at each cell to construct one-dimensional (1-D) S-velocity models. The inversion is performed for S-wave velocity using eight layers (0 – 10.55 km depth) overlying a homogeneous half-space. The initial model at each cell is taken as the last output model of the previous inverted cell, providing a natural smoothing for the entire model. Finally, the 200 best models are averaged to produce a "local" 1-D S-wave velocity structure versus depth at each cell. We then develop a 3-D distribution of shear-wave velocities using the 1-D models for all the 218 cells of our model of the Caldera. Finally, the model is linearly interpolated over the region of interest.

5. RESULTS

5.1 Double Difference Earthquake Relocation

The Menengai volcano shows a swarm of events at a depth range of 2.0 to 6.5 km. We also identify two distinct clusters of seismic events, one on the northern flank of the caldera (Cluster 1) and the other inside of the caldera (Cluster 2). The location of Cluster 2 within the Caldera is consistent with previous works on the location of the magma chamber. Specifically, a joint analysis of seismic, gravity and Magnetotellurics (MT) inversion, and petrological data for Menengai caldera (Wamalwa et al., 2013) inferred a partial melting configuration within the caldera.

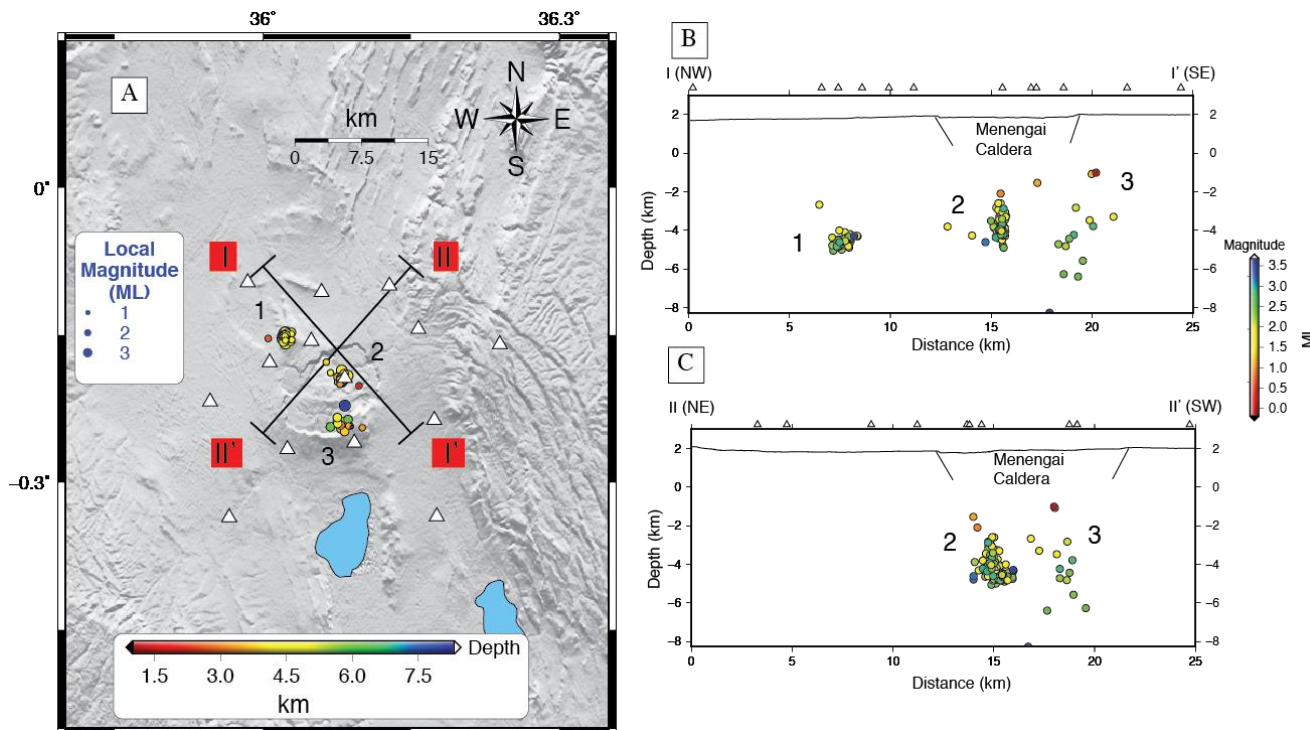


Figure 2: (A) Locations of 198 relocated hypocenters calculated by HypoDD, and detected during three-year deployment (September 2011 to January 2014). Seismic stations used to locate the events are indicated by white triangles. These events are color-coded by depth and local magnitude. (B) Topographic profile and seismic stations along transect I-I'. Seismic cluster 1 and 2 are shown in the cross-section. (C) Hypocenters along the cross-section are projected from NE-SW (II-II'). Cluster 2 and 3 are shown in this cross-section profile. The focal depth ranges 1.5 km and 8 km and magnitude range of 0.38 to 3.47.

The relocated earthquakes reveal a sharper image of seismicity composed of one cluster that extends vertically from the vent of the volcano 0 – 8 km depth (Figure 3). Then the cluster bends horizontally around a depth of 8 km – 12 km. The relative average error of the relocated events using HypoDD is significant: ± 0.19 km vertically and ± 0.14 km horizontally. These errors result from a combination of factors including, station locations, available phases, accuracy of the arrival time measurement, and cross-correlation coefficient (Waldhauser and Ellsworth, 2000). Lower crustal depths (>4 km) are common for earthquakes in the amagmatic sections of the EARS (Benson et al., 2012; Fonseca et al., 2014; Vandemeulebrouck, Roux, and Cros, 2013). Slow release of exsolving magma fluids can thus be expected at the top of the magmatic system. The concentration of shallow seismicity leading to a locally weaker upper crust is interpreted as fluid migrating and feeding the upper crustal hydrothermal system (Christopher et al., 2015; Fonseca et al., 2014; Saemundsson, 2008).

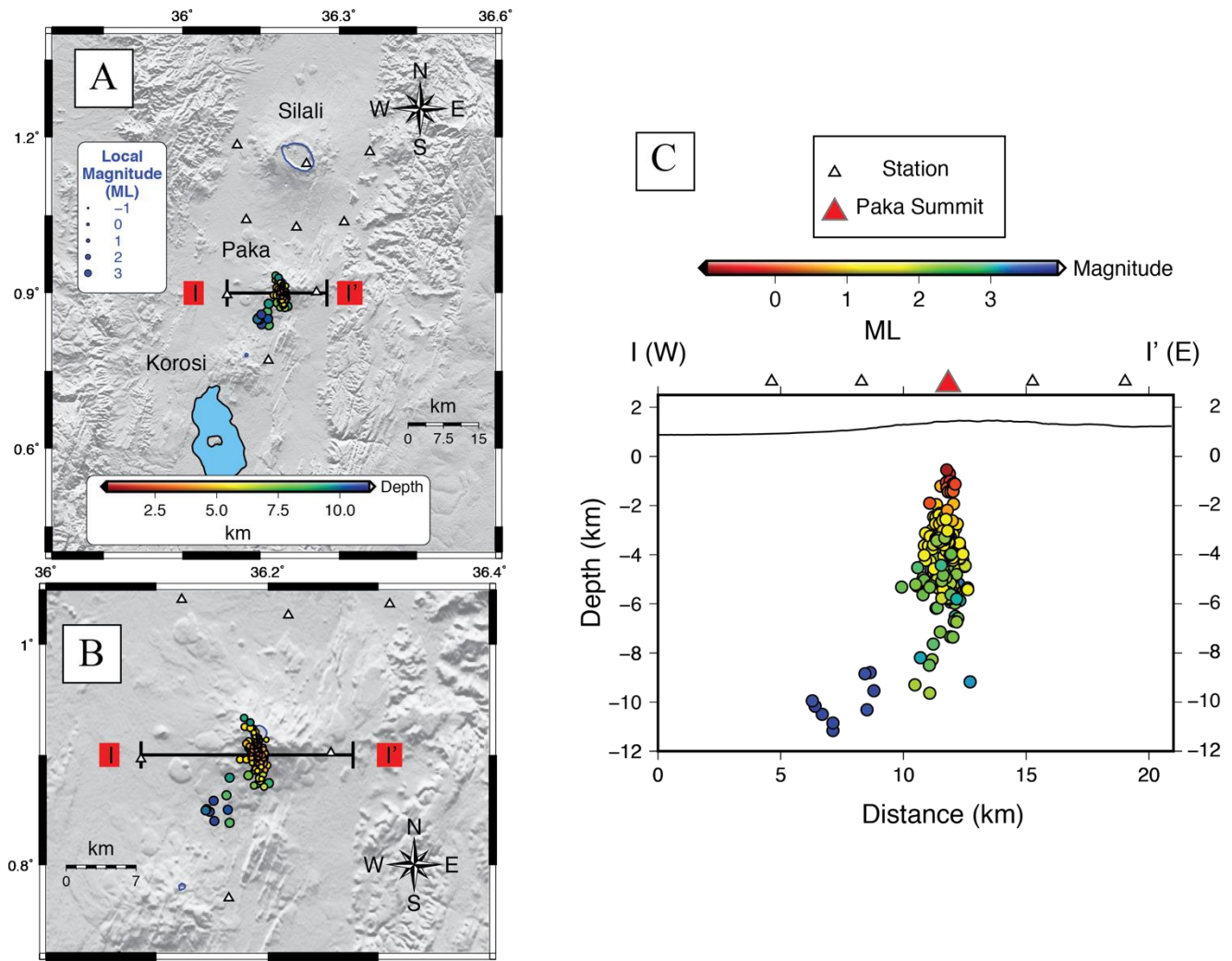


Figure 3: (A) Hypocenters of the 519 earthquakes recorded during two-year deployment (September 2012 to January 2014) at Paka volcanic center. (B) Enlarged map view of the Paka volcano. (C) Cross-section of all the epicenters ranging in local magnitude from -1 to 3.98 local magnitude.

5.2 Local Magnitude and b-value Analysis

The b-values calculated in this study are on average higher than in many other areas, where b-values have been found to range between 0.83 and 1.76. We determine separate b-values for the events for each cluster (Figure 4). For Cluster 1 and 2 at Menengai Caldera, we use the magnitude of completeness values $M_c = 2.5$ and $M_c = 2.1$, respectively. For all detected seismicity in Cluster 1 on the northwest of the flank of the Menengai caldera, $b = 1.76 \pm 0.32$; for the events beneath the Menengai caldera (Cluster 2), $b = 1.24 \pm 0.15$ (Figure 4). The b-value for Paka volcano in Cluster 1 is $b = 0.83 \pm 0.06$ using $M_c = 2.0$. Our results suggest that the shallow cluster is driven by tectonic stress, possibly triggered by magma movement from a deep intrusion. For Figure 4 and 5 both Clusters 1, the b-value is slightly above 1.0, suggesting a relatively weaker rheology, the presence of fluids and melts, the presence of highly fractured rock typical of heavily faulted caldera, and/or a higher geothermal gradient associated with the magma reservoir (Hamlyn et al., 2014). We thus interpret Cluster 2 as the region of brittle failure immediately above the magma chamber, which deforms seismically to accommodate the volume change. Several elements can affect the accuracy of the resulting b-value distribution for volcanic regions. Most are due to a large number of earthquakes in the swarms tend to increase the observed b-values that are associated with magma movement (Bridges and Gao, 2006; Sanchez et al., 2004). Thus, areas with an increased thermal gradient can be related to a weak rheology, which causes small magnitude stress changes that tend to favor more small-magnitude earthquakes compared to larger magnitude earthquakes (e.g., Farrell et al., 2009 and 2014; Murru et al., 2007). Previous work by Bridges and Gao (2006) and Sánchez et al. (2004) shows that spatial variations in b-values can impose constraints on the distribution of magma in the subsurface. The second element that can affect the observed b-values is the change in network coverage due to the addition of new stations or station failures. To our knowledge, b-values can vary between regions as different geo-mechanical properties influence the stability of rock to accumulate stress (Ibs-von Seth et al., 2001 and 2007; Utsu, 1965). Low b-values 0.5 to 0.9 can indicate that a region is capable of accumulating significant stresses, which can result in relatively large earthquakes compared to the number of smaller earthquakes (Farrell et al., 2009). Our results for Cluster 1 and 2 show evidence of the presence of high temperature and pore pressure. Sanchez et al. (2004) and

Bridges and Gao (2006) suggested vesiculation and fragmentation of ascending magma may increase b-value in the upper magmatic conduits by generating stress induced fractures (Harrinton et al., 2015; Wyss et al., 2001). However, Cluster 1 for Paka show primarily evidences low b-value associated with open cracks due to exsolution of build-up gasses or likely from regional tectonic stress conditions (Wyss et al., 2001). Another cause low b-value is fracturing of a crystalline mush similar to the carapace of a cooling lava dome (Sanchez et al., 2006).

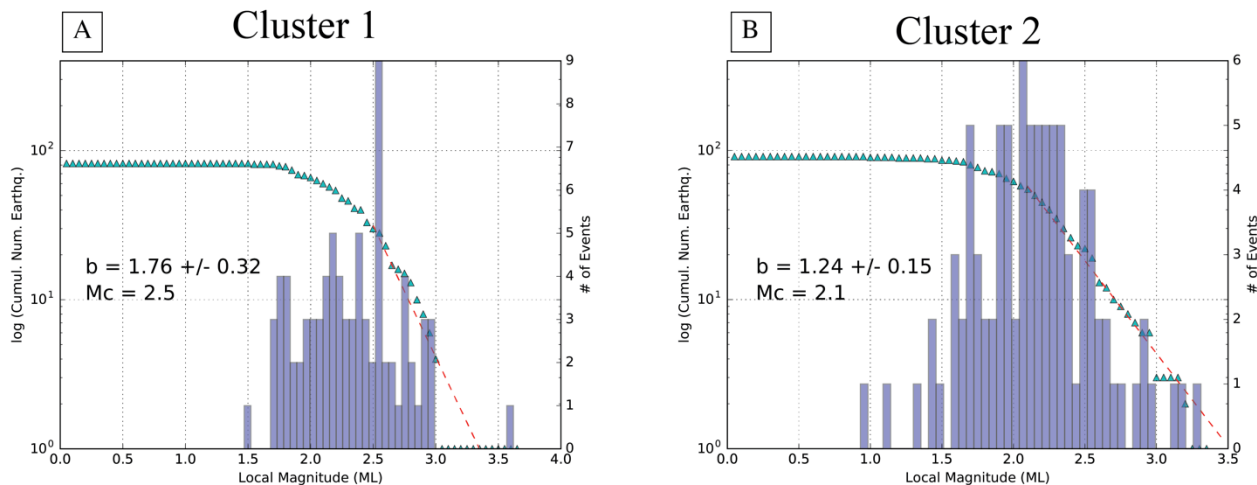


Figure 4: (A) Gutenberg-Richter distribution of relocated earthquakes on the northwest flank of Menengai caldera (Cluster 1) with the time-magnitude plot showing a peak at magnitude 2.5 and a steady decrease thereafter for bigger magnitudes. (B) Gutenberg-Richter distribution of relocated earthquakes on Menengai caldera (Cluster 2).

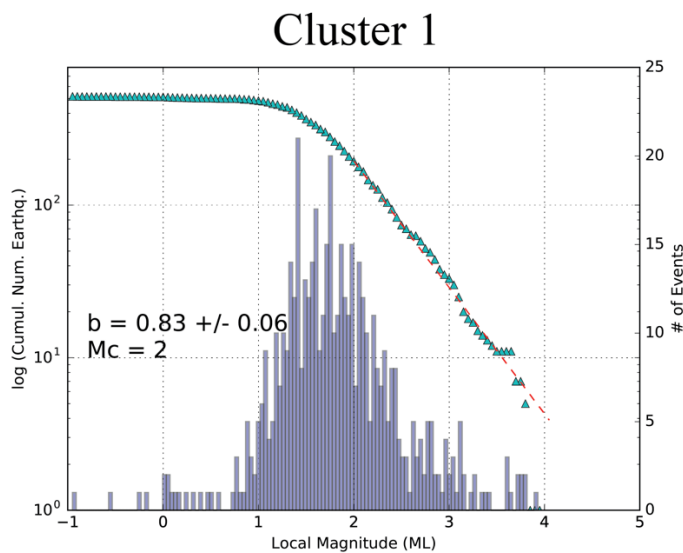


Figure 5: Gutenberg-Richter distribution of relocated earthquakes below the flank of Paka volcano for Cluster 1. The left-axis plot shows the log of the Frequency Magnitude Distribution (FMD) with magnitude completeness of 2.0 and the right-axis is a histogram depicting the number of events versus local magnitude.

5.3 Focal Mechanism

Our focal mechanism results for both clusters at Menengai caldera show a suite of solutions, dominated by transtensive and transpressive mechanisms (Figure 6). The different orientations of the fault planes for both clusters suggest that there are thrust and/or normal faults responsible for the clusters, which is consistent with the events resulting from magma movement below. Cluster 2 events show a small number of both thrust and normal faults with a suggestion of nodal planes striking NE-SW, which can be interpreted as the movement of the magma chamber been pulling and pushing the upper shallow crust (Taddeucci et al., 2013; Feuillet, 2013). The thrust mechanisms likely result from magma pushing upward through the system, while the normal mechanisms are likely readjustments to the new stress field created by the magma.

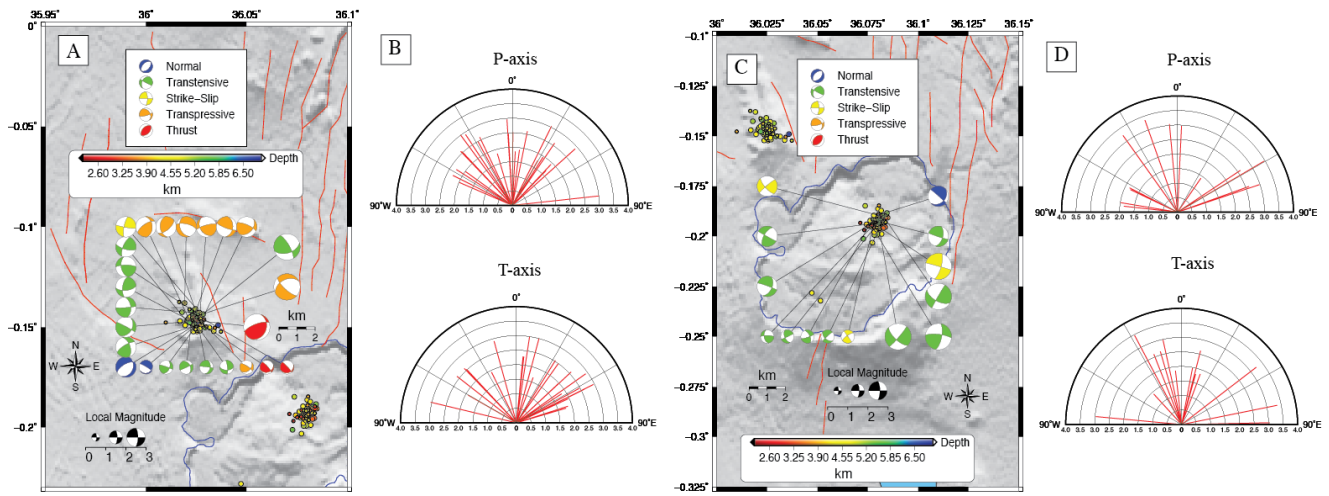


Figure 6: (A) Lower hemisphere fault plane solutions for 25 earthquakes in cluster 1; the location of the corresponding hypocenter (color-coded with depth). The color-coded fault plane solution corresponds with different classification of focal mechanisms. The size of the fault plane solution is related to the magnitude of the event, and the color of the compressional quadrant of the solution is related to its depth. Blue outline highlights the caldera region. Red lines indicate the tectonic faults associated with the rift system (Ryan et al., 2009). (A Right) P-axis and T-axis orientations, both illustrate the red plunges lines for each focal mechanism. (B) Lower hemisphere fault plane solutions for 14 earthquakes of cluster 2. (B Right) P-axis and T-axis orientations, both illustrate the red plunges lines for each focal mechanism and the blue color is the total average.

Our results show different distributions of fault plane solution that are too complex to define a major fault system in the rift systems (Tongue et al., 1994). Our complex distribution appears to be governed by regional tectonics and local magmatic effects on the stresses. The focal mechanisms show the orientation in the T-axis minimum compressional stress for the normal faults with similar nodal plane orientation that align with regional tectonic stresses associated with the rift system. For example, the thrust faults strike in an eastward direction with the normal faults striking NW-SE. Focal mechanisms for Paka show predominantly thrust faulting with the nodal plane striking NE-SW (Figure 7). Tongue et al. (1994) suggested in their focal mechanism analysis the presence of sub-vertical, N-S trending fault planes in the hypocentral region and a WNW-ESE directed extensional stress field. The rift center is characterized by recent volcanism and geothermal activity. We suggest our results associated with N-trending faults and fissure fed by a linear magma chamber and modulated by regional tectonic stresses producing complex distribution of fault solution (Ibs-von Seht et al., 2001; Tonguen et al., 1994). The parallelism suggests normal faulting on the N-trending faults and is thus consistent with extensional stress conditions (Statz-Boyer et al., 2009).

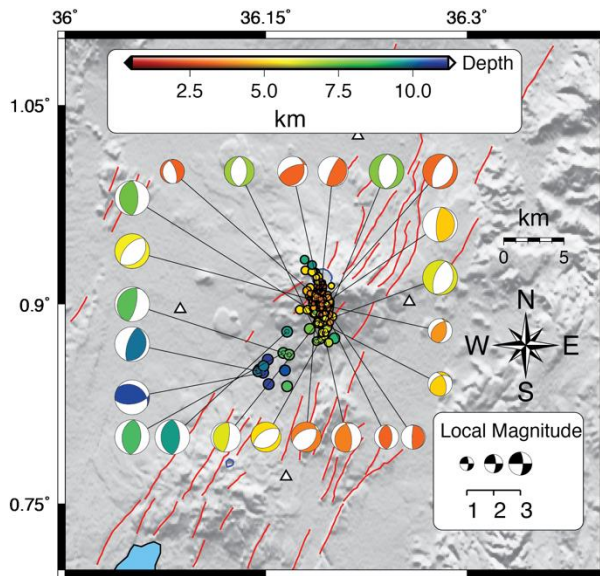


Figure 7: Lower hemisphere fault plane solutions for 22 earthquakes in Cluster 1; hypocenters color-coded by depth; size of the fault plane solution is scaled to the local magnitude of the event, and the color of the compressional quadrant of the solution is related to its depth in kilometers. Blue lines outline the volcanic region. Red traces outline the tectonic faults associated with the rift system (Ryan et al., 2009).

5.4 Ambient Noise Tomography

We found a shallow and deep low velocity anomaly beneath the Menengai Caldera (Figure 8). Based on KRISP 85 and 90 rift axial model, Simiyu and Keller (2000) identified a deep anomaly at depth of 5-7 km. Another study from Simiyu (2010) applied a travel-time tomography and described evidence of high V_p/V_s ratio locate at the summit of Menengai Caldera. Gravity inversion carried out by Simiyu and Keller 2001 identified a density anomaly $2.90 \times 10^3 \text{ kgm}^{-3}$ at a depth of 2.5 km that corresponds to the magma chamber of Menengai. Our results agree with Simiyu (2010) for our deep anomaly beneath the Menengai Caldera. The shallow magma intrusion present at a depth of 0-1km (anomaly (A) in Figure 8) correlates well with Simiyu and Keller (2001) work. They implemented gravity models and active source experiment used from KRISP experiment in 1985 and 1990 that cover central and south of the Kenya rift. Another finding from Simiyu (2010) and Simiyu and Keller (2000) is a deep anomaly that correlates with anomaly (B) in Figure 8. Simiyu (2010) identified the heat source below the hydrothermal reservoir as ranging from 4–7 km, which coincides with our location of the magma chamber. Two clusters are visible in the spatial distribution of the earthquakes in Figure 8: Cluster 1 is located NW of the flank of Menengai caldera and forms a spherical cluster with a depth of 3 km - 6 km, and Cluster 2 forms a subvertical elongated cluster that lies beneath the summit crater with a depth of 2 km – 6 km. In Figure 8 Cluster 1 shows evidence that the hypocenters are located around high shear wave velocities that are interpreted as an ancient magma reservoir at north of the flank of the caldera (Wamalwa et al., 2013). Our results show traces of high shear wave velocity in Cluster 2 ranging from 2.0 km/s – 2.4 km/s. Cluster 2 lies beneath the caldera and this evidence implies two regions of slow shear wave velocities are between the hypocenter swarms. Exsolving magma fluids can thus be expected at the top of the magmatic system. The concentration of shallow seismicity leading to a locally weaker upper crust is interpreted as fluid migrating and feeding the upper crustal magma system (Christopher et al., 2015; Fonseca et al., 2014; Saemundsson, 2008; Vargas-Bracamontes and Neuberg, 2012).

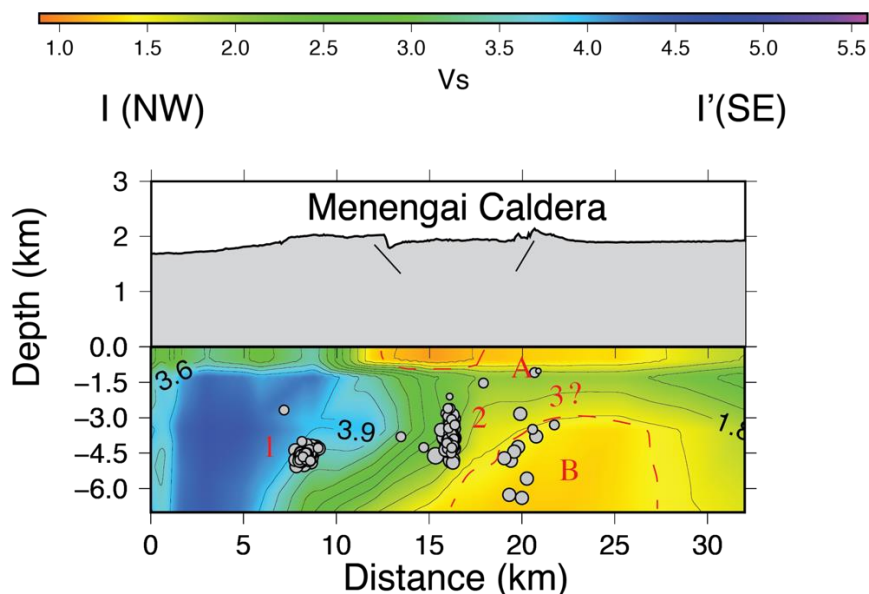


Figure 8: NW-SE (I-I') cross-sections (see Figure 2) showing 3-D tomography of Menengai Caldera. Two major low velocity zone (A and B) are beneath the Menengai Caldera. Three seismic swarm (gray circles) are superimposed with the 3-D tomography (grey dots scaled by magnitude).

Figure 9 shows a profile that crosses Silali, which depicts a low S-wave velocity region directly beneath the volcano rim at a depth of about 6 km. The ray coverage for the Silali volcano traces only half of the rim of Silali due to the small number of stations in the seismic network. We call this anomaly A. Figure 10, centered at Paka, shows a cross section (B-B') with a shear wave velocity anomaly to the east of the volcanic center at a depth of about ($>2.25 \text{ km/s}$). Our results correlate with our high shear velocity beneath Paka volcano. However, smearing is present at the dome volcanoes where the azimuth distribution of rays is poor north and south. This result may be a hot deep fluids to shallow depths, but due to the limited ray path resolution it is difficult to determine the correct size and location of the anomaly. There is evidence of active hot springs, hot grounds, fumaroles, and steam jets located along the shore of Lake Bogoria, Arus volcano, and to the north of the Menengai caldera (Simiyu 2009; Simiyu 2010). This magma chamber could be feeding both patches of magma reservoirs at Korosi volcano, implying that there is a pathway connecting this deep anomaly to the surface.

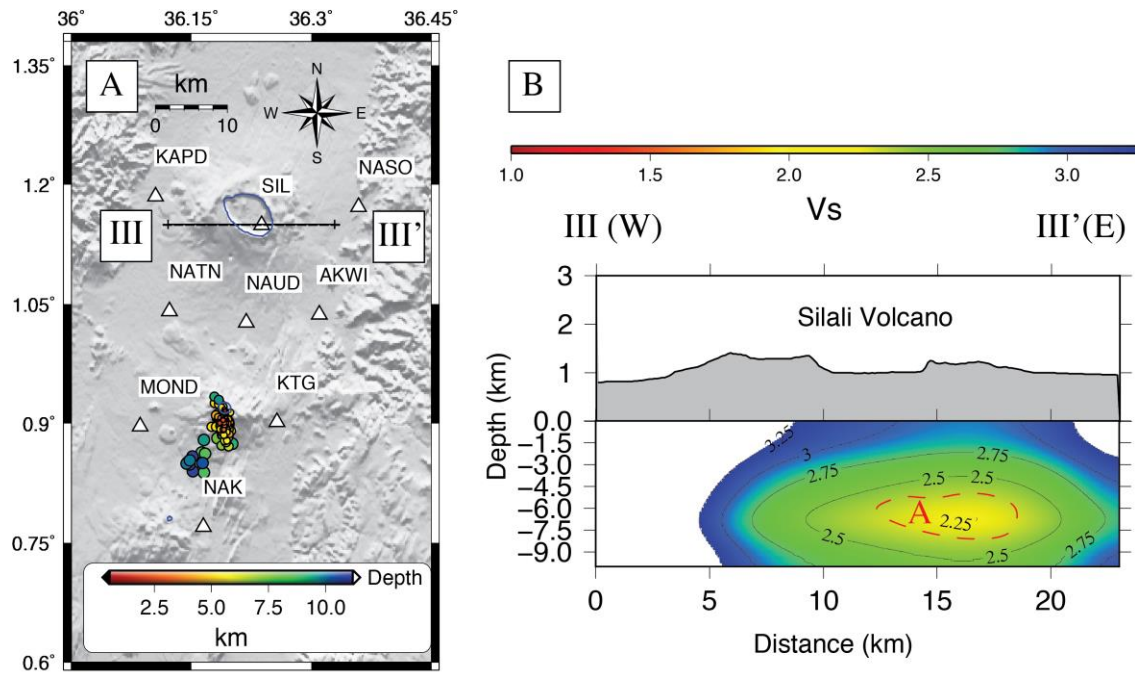


Figure 9: (A) Map shows the seismic network, but we did not find any seismicity near Silali during the temporary deployment. (B) Topographic profile, and cross-section (III-III') showing 3-D tomography of Silali.

Simiyu (2010), Mbia et al. (2014), and Young et al. (1991) suggest the fluid migrates to the subsurface as the magma chamber is heating up (Figure 10 and 11). The tomographic studies showed a magma reservoir at a depth of 1.5–4 km. Our results using ANT correlated with the (MT) by Shako and Mutua (2012) and Kangogo et al. (2011), show the heat source signatures or magma reservoir present at a depth of 0 – 7.5 km Korosi volcano. Figures 8 shows evidence that the hypocenters between 4 to 5 km depth are located around regions of high shear wave velocity that are interpreted as an ancient magma reservoir forming a brittle failure cloud that reopens a new pathway for future residual magma to migrate within the subsurface (Wamalwa et al., 2013). Our results show traces of high shear wave velocity in Cluster 2 ranging from 2.4 km/s – 3.0 km/s. The cluster shows traces of brittle failure opening a pathway for migrating gas or hot fluid. The anomaly C is located next to Paka volcano and eastward of Korosi volcano (Figure 11). No magma reservoir anomaly is found beneath the seismicity cluster under Paka volcano. We interpret this anomaly as deep fluid migrating and feeding the upper crustal magma system away or from the flank of Korosi and Paka volcano (Christopher et al., 2015; Fonseca et al., 2014; Saemundsson, 2008).

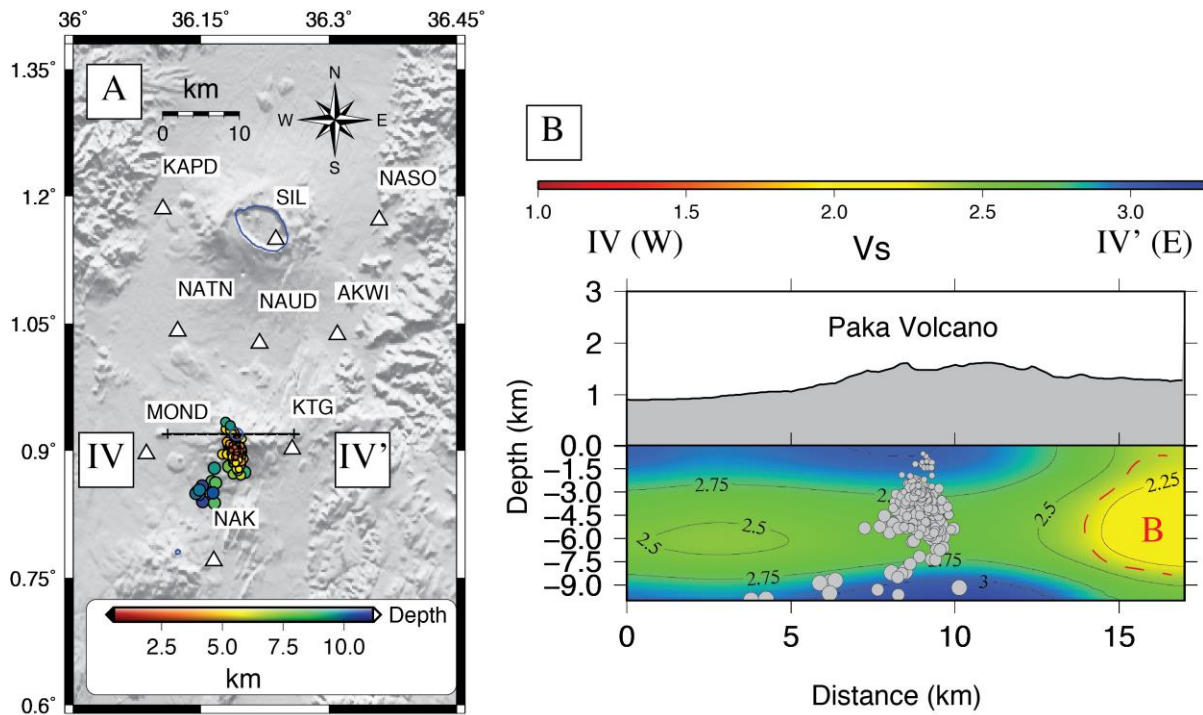


Figure 10: (A) Map showing the seismic network with seismicity beneath the Paka volcano. (B) Topographic profile, and a cross-section (IV-IV') at the Paka volcano. The seismicity is shown as gray dots scaled by magnitude. Low shear velocity is shown in light yellow color and high shear velocity shown in blue.

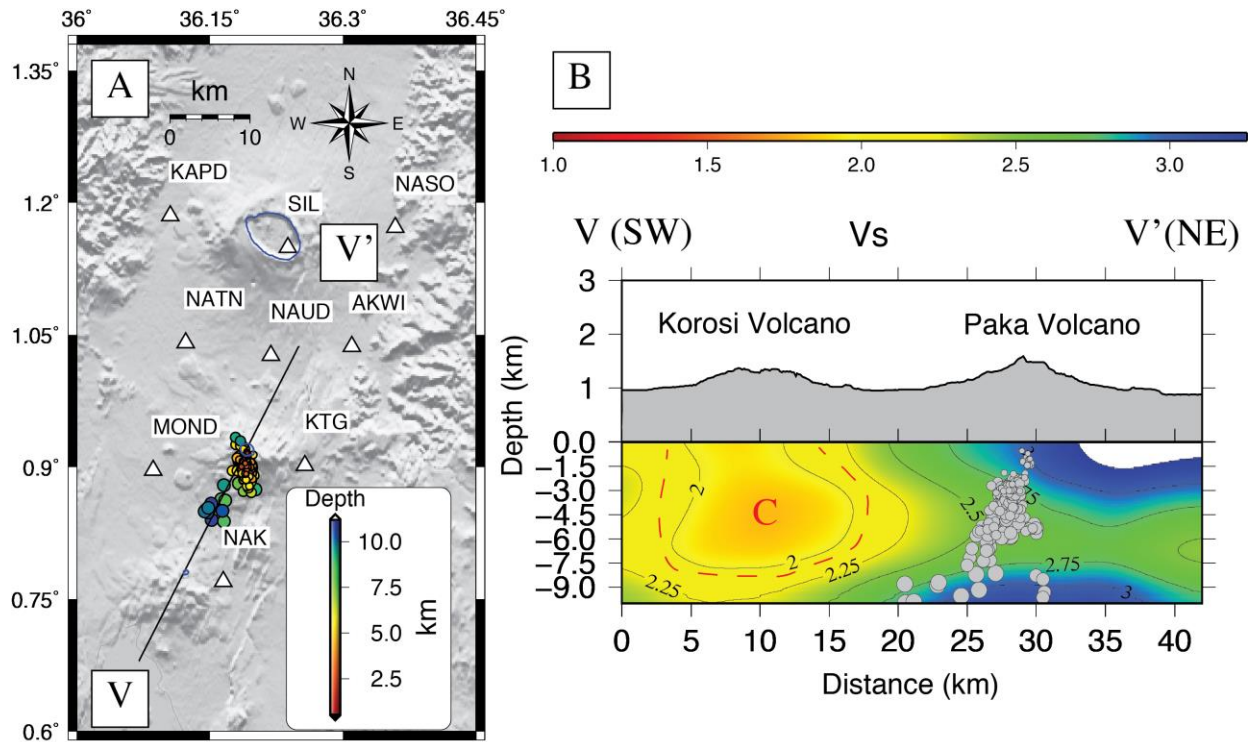


Figure 11: (A) Map coverage of the seismic network showing the trace line of the cross section for (V-V'). (B) SW-NE (V-V') cross-section showing 3-D tomography of Korosi and Paka volcano. The seismicity are shows in gray color dots (scaled by magnitude). Colored contour show shear wave velocity with one anomaly (C); low velocity in yellow, high velocity in blue.

6. CONCLUSION

In this paper, we analyze seismicity from a three-year deployment of a broadband seismic network in the EARS in order to identify magma reservoirs and investigate the volcanic processes of a transmitted system in Kenya. We calculate high-resolution earthquake locations, magnitudes, determined focal mechanisms, and perform a *b*-value analysis to better understand the stresses of magma chambers or fault zones. We found three distinct clusters of seismic events, one inside the caldera and one on the northern flank, and last one beneath Paka volcano. The location of the cluster within the Menengai caldera is consistent with previous work Simiyu (2010) and Wamalwa et al. (2013) and our results correlate with the stress analysis and tomography. Majority of our results from focal mechanism, show a mixture of normal, thrust, transtensional, and transpressional fault zone favor to rift spreading and local stress fields that may favor formation of the vent at the base of the volcano (Mathieu et al., 2011). We suggest four shallow magma source can be identified below the crater of Menengai caldera and Silali, Paka, and Korosi. We identify shallow magma reservoir beneath Korosi using the 14 seismic stations around the Menengai Caldera and nine stations at the volcanic centers. We detect a swarm of seismicity beneath Paka and a low *S* velocity anomaly is identified east of the flank of Paka at a depth of 3-6 km. We suggest the magma reservoir is migrating to the Paka volcano. The stress analysis shows strong evidence of high *b*-values correlating with high thermal gradient beneath Paka volcano. Focal mechanisms at Paka suggest the *P*-axis is striking NE-SW and are indicative of faulting being controlled by local stresses and tectonic regional stress. At Silali volcano, we identify a deep magma chamber using ANT, but no seismicity was recorded during the study. We conclude that active fluid movement under Menengai and Paka indicated by seismicity and low *S*-wave velocity suggest potential for geothermal production at these sites.

REFERENCES

- Albaric, J., J. D'everch`ere, J. Perrot, A. Jakovlev, and A. Deschamps (2014), Deep crustal earthquakes in North Tanzania, East Africa: Interplay between tectonic and magmatic processes in an incipient rift, *Geochem. Geophys. Geosyst.*, *15*, 374-394, doi: 10.1002/2013GC005027.
- Andronicos, C. L., A. A. Velasco, and J. M. Hurtado (2007), Large-scale deformation in the India-Asia collision constrained by earthquakes and topography, *Terra Nova*, *19*(2), 105-119, doi:10.1111/j.1365-3121.2006.00714.x.
- Bagley, B., and A. A. Nyblade (2013), Seismic anisotropy in eastern Africa, mantle flow, and the African superplume, *Geophys. Res. Lett.*, *40*, 1500-1505, doi:10.1002/grl.50315.
- Begg, G. C., W. L. Griffin, L. M. Natapov, S. Y. O'Reilly, S. P. Grand, C. J. O'Neill, J. M. A. Hronsky, Y. P. Djomani, C. J. Swain, T. Deen, and P. Bowden (2009), The lithospheric architecture of Africa: Seismic tomography, mantle petrology, and tectonic evolution, *Geosphere*, *5*, no.1, 23-50
- Bensen, G. D., M. H. Ritzwoller, M. P. Barmin, A. L. Levshin, F. Lin, M. P. Moschetti, N. M. Shapiro, and Y. Yang (2007), Processing seismic ambient noise data to obtain reliable broad-band surface wave dispersion measurements, *Geophysical Journal International*, *169*(3), 1239-1260.
- Benson, P. M., M. J. Heap, Y. Lavallée, A. Flaws, K.-U. Hess, A.P.S. Selvadurai, D. B. Dingwell, B. Schillinger, (2012), Laboratory simulations of tensile fracture development in a volcanic conduit via cyclic magma pressurisation, *Earth and Planetary Science Letters*, Vol. 349-350, 231-239, ISSN 0012-821X, <http://dx.doi.org/10.1016/j.epsl.2012.07.003>.
- Biggs, J., E. Y. Anthony, and C. J. Ebinger (2009), Multiple inflation and deflation events at Kenyan volcanoes, East Africa Rift, *Geology*, v. 37, no. 11, 979-982.
- Bridges, D. L., and S. S. Gao (2006), Spatial variation of seismic *b*-values beneath Makushin Volcano, Unalaska Island, Alaska, *Earth and Planetary Science Letters*, *245*(1), 408-415.
- Campillo, M., and A. Paul (2003), Long-range correlations in the diffuse seismic coda, *Science*, *299*, 547-549.
- Chorowicz J. (2005), The east African rift system, Elsevier: *Journal of African Earth Sciences*, *43*, 379-410.
- Christopher, T. E., J. Blundy, K. Cashman, P. Cole, M. Edmonds, P. J. Smith, R. S. J. Sparks, and A. Stinton (2015), Crustal-scale degassing due to magma system destabilization and magma-gas decoupling at Soufrière Hills Volcano, Montserrat, *Geochem. Geophys. Geosyst.*, n/a-n/a, doi:10.1002/2015GC005791.
- Clarke, M.C.G., D.G. Woodhall, (1987), Geological and geothermal mapping. British Survey, Exploration for Geothermal Energy Project, Progress report BGSKEN/2, 135 pp.
- Ebinger, C. J., D. Keir, A. Ayele, E. Calais, T. J. Wright, M. Belachew, J. O. S. Hammond, E. Campbell, and W. R. Buck (2008), Capturing magma intrusion and faulting processes during continental rupture: seismicity of the Dabbahu (Afar) rift, *Geophysical Journal International*, *174*(3), 1138-1152, doi:10.1111/j.1365-246X.2008.03877.x.
- Ebmeier, S. K., J. Biggs, T. A. Mather, and F. Amelung (2013), On the lack of InSAR observations of magmatic deformation at Central American volcanoes, *J. Geophys. Res. Solid Earth*, *118*(5), 2571-2585, doi:10.1002/jgrb.50195.
- Fang, H., H. Yao, H. Zhang, Y.-C. Huang, and R. D. van der Hilst (2015), Direct inversion of surface wave dispersion for three-dimensional shallow crustal structure based on ray tracing: methodology and application, *Geophys. J. Int.*, *201*(3), 1251-1263, doi:10.1093/gji/ggv080.

- Farrell, J., R. B. Smith, S. Husen, and T. Diehl (2014), Tomography from 26 years of seismicity revealing that the spatial extent of the Yellowstone crustal magma reservoir extends well beyond the Yellowstone caldera, *Geophysical Research Letters*, *41*(9), 3068–3073, doi:10.1002/2014GL059588.
- Farrell, J., S. Husen, and R. B. Smith (2009), Earthquake swarm and b-value characterization of the Yellowstone volcano-tectonic system, *Journal of Volcanology and Geothermal Research*, *188*(1–3), 260–276, doi:10.1016/j.jvolgeores.2009.08.008.
- Feuillet, N. (2013), The 2011–2012 unrest at Santorini rift: Stress interaction between active faulting and volcanism, *Geophys. Res. Lett.*, *40*, 3532–3537, doi:10.1002/grl.50516.
- Fonseca, J. F. B. D., J. Chamussa, A. Domingues, G. Helffrich, E. Antunes, G. van Aswegen, L. V. Pinto, S. Custodio, and V. J. Manhica (2014), MOZART: A Seismological Investigation of the East African Rift in Central Mozambique, *Seismological Research Letters*, *85*(1), 108–116, doi:10.1785/0220130082.
- Garbin M., E. Priolo (2013), Seismic Event Recognition in the Trentino Area (Italy): Performance Analysis of a New Semiautomatic System, *Seismol. Res. Lett.*, *84*, no. 1, 65–74. doi: 10.1785/0220120025.
- Goutorbe, B., D. L. de O. Coelho, and S. Drouet (2015), Rayleigh wave group velocities at periods of 6–23 s across Brazil from ambient noise tomography, *Geophys. J. Int.*, *203*(2), 869–882, doi:10.1093/gji/ggv343.
- Gutenberg, B., and C. F. Richter (1944), Frequency of earthquakes in California, *Bulletin of the Seismological Society of America*, *34*(4), 185–188.
- Halldórsson, S. A., D. R. Hilton, P. Scarsi, T. Abebe, and J. Hopp (2014), A common mantle plume source beneath the entire East African Rift System revealed by coupled helium-neon systematics, *Geophys. Res. Lett.*, *41*, 2304–2311, doi: 10.1002/2014GL059424.
- Hamlyn, J. E., D. Keir, T. J. Wright, J. W. Neuberg, B. Goitom, J. O. S. Hammond, C. Pagli, C. Oppenheimer, J.-M. Kendall, and R. Grandin (2014), Seismicity and subsidence following the 2011 Nabro eruption, Eritrea: Insights into the plumbing system of an off-rift volcano, *Journal of Geophysical Research: Solid Earth*, *119*(11), 8267–8282, doi:10.1002/2014JB011395.
- Hardebeck, J. L., and P. M. Shearer (2002), A new method for determining first-motion focal mechanisms, *Bulletin of the Seismological Society of America*, *92*(6), 2264–2276.
- Hardebeck, J. L., and P. M. Shearer (2003), Using S/P amplitude ratios to constrain the focal mechanisms of small earthquakes, *Bulletin of the Seismological Society of America*, *93*(6), 2434–2444.
- Harrington, R. M., G. Kwiatek, and S. C. Moran (2015), Self-similar rupture implied by scaling properties of volcanic earthquakes occurring during the 2004–2008 eruption of Mount St. Helens, Washington, *J. Geophys. Res. Solid Earth*, *120*(7), 2014JB011744, doi:10.1002/2014JB011744.
- Hermann, R.B., and C. J. Ammon (2004), surf96 from computers programs in seismology, surface waves, receiver functions and crustal structure, version 3.30, Department of Earth and Atmospheric Sciences, Saint Louis University.
- Ibs-von Seht, M., S. Blumenstein, R. Wagner, D. Hollnack, and J. Wohlenberg (2001), Seismicity, seismotectonics and crustal structure of the southern Kenya Rift—new data from the Lake Magadi area, *Geophysical Journal International*, *146*(2), 439–453.
- Ibs-von Seht, M., T. Plenefisch, and K. Klinge (2008), Earthquake swarms in continental rifts—a comparison of selected cases in America, Africa and Europe, *Tectonophysics*, *452*(1), 66–77.
- Kangogo, D., J. Gichira, A. Wamalwa, C. Simiyu, and Y. Noor (2011), Resistivity structure of Silali geothermal prospect in Kenya, Kenya International Conference Centre, Nairobi, November 21–23,
- Keller, G. R., M. A. Khan, P. Morganc, R. F. Wendlandt, W. S. Baldrige, K. H. Olsen, C. Prodehl, and L. W. Braile (1991), A comparative study of the Rio Grande and Kenya rifts, *Tectonophysics*, *197*(2), 355–371.
- Kennett, B. L. N., and E. R. Engdahl (1991). Traveltimes for global earthquake location and phase identification. *Geophysical Journal International* *122*, 429–465.
- Kim, K., A. A. Nyblade, J. Rhie, C. Baag, and T.S. Kang (2012), Crustal S-wave velocity structure of the Main Ethiopian Rift from ambient noise tomography, *Geophysical Journal International*, *191*, 865–878.
- Larson, K. M. (2013), A new way to detect volcanic plumes, *Geophys. Res. Lett.*, *40*, 2657–2660, doi:10.1002/grl.50556.
- Levshin, A.L., V. F. Pisarenko, and G. A. Pogrebinsky (1972), On a frequency-time analysis of oscillations, *Ann. Geophys.*, *28*, 211–218.
- Lippitsch, R., R. S. White, and H. Soosalu (2005), Precise hypocentre relocation of microearthquakes in a high-temperature geothermal field: the Torfajökull central volcano, Iceland, *Geophys. J. Int.*, *160*(1), 370–387, doi:10.1111/j.1365-246X.2005.02467.x.
- Mathieu, L., B. van W. de Vries, M. Pilato, and V. R. Troll (2011), The interaction between volcanoes and strike-slip, transtensional and transpressional fault zones: Analogue models and natural examples, *Journal of Structural Geology*, *33*(5), 898–906.

- Mbia, P. K., A. K. Mortensen, N. Oskarsson, and S. Bjorn (2014), Sub-Surface Geology, Petrology and Hydrothermal Alteration of the Menengai Geothermal Field, Kenya: Case Study of Wells MW-02, MW-04, MW-06 and MW-07, Master thesis, University of Iceland, Reykjavik.
- Molnar, P., and Y. P. Aggarwal (1971), A microearthquake survey in Kenya, *Bulletin of the Seismological Society of America*, 61(1), 195–201.
- Mulibo, G. D., and A. A. Nyblade (2009), The 1994–1995 Manyara and Kwamtoro earthquake swarms: Variation in the depth extent of seismicity in Northern Tanzania, *South African Journal of Geology*, 112(3–4), 387–404.
- Mulibo, G. D., and A. A. Nyblade (2013), Mantle transition zone thinning beneath eastern Africa: Evidence for a whole-mantle superplume structure, *Geophys. Res. Lett.*, 40, 3562–3566, doi:10.1002/grl.50694.
- Murru, M., R. Console, G. Falcone, C. Montuori, and T. SgROI (2007), Spatial mapping of the b value at Mount Etna, Italy, using earthquake data recorded from 1999 to 2005, *J. Geophys. Res.*, 112(B12), B12303, doi:10.1029/2006JB004791.
- Nicolson, H., A. Curtis, B. Baptie, and E. Galetti, (2012), Seismic interferometry and ambient noise tomography in the British Isles, *Proceeding of the Geologist's Association*, 123, 74–86.
- Pasyanos, M. E. (2008), Lithospheric thickness modeled from long period surface wave dispersion, *Tectonophysics*, 481, iss. 1–4, 38–50.
- Pasyanos, M. E. and A. A. Nyblade (2007), A top to bottom lithospheric study of Africa and Arabia, *Tectonophysics*, 444, 27–44.
- Roberts, E. M., N. J. Stevens, P. M. O'Connor, P. H. G. M. Dirks, M. D. Gottfried, W. C. Clyde, R. A. Armstrong, A. I. S. Kemp, S. Hemming (2012), Initiation of the western branch of the East African Rift coeval with the eastern branch, *Nature Geoscience*, 5, 289–294.
- Rooney, T. O., I. D. Bastow, D. Keir, F. Mazzarini, E. Movsesian, E. B. Grosfils, J. R. Zimelman, M. S. Ramsey, D. Ayalew, and G. Yirgu (2014), The protracted development of focused magmatic intrusion during continental rifting: focused magma intrusion during rifting, *Tectonics*, 33(6), 875–897, doi:10.1002/2013TC003514.
- Ryan, W.B.F., S.M. Carbotte, J.O. Coplan, S. O'Hara, A. Melkonian, R. Arko, R.A. Weissel, V. Ferrini, A. Goodwillie, F. Nitsche, J. Bonczkowski, and R. Zemsky (2009), *Global Multi-Resolution Topography synthesis*, *Geochem. Geophys. Geosyst.*, 10, Q03014, doi:10.1029/2008GC002332.
- Saemundsson, K. (2008), East African rift system. An overview, *Short Course III, UNU-GTP, Lake Naivasha, Kenya*.
- Sánchez, J. J., S. R. McNutt, J. A. Power, and M. Wyss (2004), Spatial variations in the frequency-magnitude distribution of earthquakes at Mount Pinatubo volcano, *Bulletin of the Seismological Society of America*, 94(2), 430–438.
- Shako, L. and J. Mutua (2012), Evaluation of the Geothermal Potential for Korosi/Chepchuk Prospect, Kenya, Using GIS, *GRC Transactions*, Vol. 36.
- Simiyu, S. M., (2009), Application of micro-seismic method to geothermal exploration from the Kenya Rift: U. N. Short Course for Exploration for Geothermal Resources.
- Simiyu, S., and G. R. Keller, (2000), Seismic monitoring of the Olkaria geothermal area, Kenya rift valley. *Journal of Volcanology and Geothermal Research*, 95: 1–4.
- Simiyu, S., and G. R. Keller, (2001), An integrated geophysical analysis of the upper crust of the southern Kenya rift. *Geophysical Journal International*. 147: 543–561.
- Spica, Z., D. Legrand, A. Iglesias, T. R. Walter, S. Heimann, T. Dahm, J.-L. Froger, D. Rémy, S. Bonvalot, and M. West (2015), Hydrothermal and magmatic reservoirs at Lazufre volcanic area, revealed by a high-resolution seismic noise tomography, *Earth and Planetary Science Letters*, 421, 27–38, doi:10.1016/j.epsl.2015.03.042.
- Statz-Boyer, P., C. Thurber, J. Pesicek, and S. Prejean (2009), High precision relocation of earthquakes at Iliamna Volcano, Alaska, *Journal of Volcanology and Geothermal Research*, 184(3–4), 323–332, doi:10.1016/j.jvolgeores.2009.04.016.
- Taddeucci, J., G. A. Valentine, I. Sonder, J. D. L. White, P.-S. Ross, and P. Scarlato (2013), The effect of pre-existing craters on the initial development of explosive volcanic eruptions: An experimental investigation, *Geophys. Res. Lett.*, 40, 507–510, doi: 10.1002/grl.50176.
- Tarasewicz, J., B. Brandsdóttir, R. S. White, M. Hensch, and B. Thorbjarnardóttir (2012), Using microearthquakes to track repeated magma intrusions beneath the Eyjafjallajökull stratovolcano, Iceland: TRACKING INTRUSIONS AT EYJAFJALLAJÖKULL, *Journal of Geophysical Research: Solid Earth*, 117(B9), n/a–n/a, doi:10.1029/2011JB008751.
- Tongue, J. A. (1992), Tomographic study of local earthquake data from the Lake Bogoria region of the Kenya Rift Valley, *Geophysical Journal International*, 109(2), 249–258.
- Tongue, J., P. Maguire, and P. Burton (1994), An earthquake study in the Lake Baringo basin of the central Kenya Rift, *Tectonophysics*, 236(1–4), 151–164.

- Utsu, T. (1965), A method for determining the value of b in a formula $\log n = a - bM$ showing the magnitude-frequency relation for earthquakes, *Geophys. Bull. Hokkaido Univ.*, 13, 99-103.
- Vandemeulebrouck, J., P. Roux, and E. Cros (2013), The plumbing of Old Faithful Geyser revealed by hydrothermal tremor, *Geophys. Res. Lett.*, 40, 1989-1993, doi: 10.1002/grl.50422.
- Vargas-Bracamontes, D. M., and J. W. Neuberg (2012), Interaction between regional and magma-induced stresses and their impact on volcano-tectonic seismicity, *Journal of Volcanology and Geothermal Research*, 243-244, 91-96, doi:10.1016/j.jvolgeores.2012.06.025.
- Velasco, A., G. Kaip, A. Wamalwa, E. Patlan (2011), Seismic Characterization of Menengai Crater, Kenya. International Federation of Digital Seismograph Networks. Other/Seismic Network. doi:10.7914/SN/1C_2011
- Waldhauser, F., and W. L. Ellsworth (2000), A double-difference earthquake location algorithm: Method and application to the northern Hayward fault, California, *Bulletin of the Seismological Society of America*, 90(6), 1353-1368.
- Walker, K. T., A. A. Nyblade, S. L. Klemperer, G. H. R. Bokelmann, and T. J. Owens (2004), On the relationship between extension and anisotropy: Constraints from shear wave splitting across the East African Plateau, *J. Geophys. Res.*, 109.
- Wamalwa, A., K. Mickus, and L. Serpa (2013), Geophysical characterization of the Menengai volcano, Central Kenya Rift from the analysis of magnetotelluric and gravity data, *GEOPHYSICS*, 78(4), B187-B199, doi:10.1190/geo2011-0419.1.
- Williams L. A. J., R. Macdonald, and G. R. Chapman (1984), Late Quaternary caldera volcanoes of the Kenya rift valley, *Journal of Geophysical Research*, 89(B10), 8553-8570.
- Wyss, M., F. Klein, K. Nagamine, and S. Wiemer (2001), Anomalously high b-values in the South Flank of Kilauea volcano, Hawaii: evidence for the distribution of magma below Kilauea's East rift zone, *Journal of Volcanology and Geothermal Research*, 106(1), 23-37.
- Yang, Y., M. H. Ritzwoller, and C. H. Jones (2011), Crustal structure determined from ambient noise tomography near the magmatic centers of the Coso region, southeastern California, *Geochemistry Geophysics Geosystems*, 12,1-20
- Yang, Y., W. Shen, and M. H. Ritzwoller (2011), Surface wave tomography on a large- scale seismic array combining ambient noise and teleseismic earthquake data, *Earthquake Sciences*, 24, 55-64
- Young, P. A. V., P. K. H. Maguire, N. d'A Laffoley, and J. R. Evans (1991), Implications of the distribution of seismicity near Lake Bogoria in the Kenya Rift, *Geophysical Journal International*, 105(3), 665-674.